Macromolecules

pubs.acs.org/Macromolecules
Article

Rational Design of New Biocompatible Near-Infrared Conjugated Polymer Nanoparticles for Biomedical Applications

Aristea Pavlou, Athanasios Katsouras, Maria Markou, Alkmini Nega, Sofia Bellou, Panagiota Koralli, Andriana Schiza, Nikolaos Chalmpes, Vasilis G. Gregoriou, Antonia Dimitrakopoulou-Strauss, Theodore Fotsis, Apostolos Avgeropoulos, Michael G. Siskos, Carol Murphy, and Christos L. Chochos*

Cite This: Macromolecules 2026, 59, 1429−1442

ABSTRACT: Conjugated polymer nanoparticles (CPNs) have gained significant attention as promising nanomaterials for cancer theranostics, particularly in fluorescence imaging and therapy, where early detection and image-guided surgery are crucial for effective treatment. Despite growing interest, there remains a notable gap in the literature regarding rational design strategies and clear structure−property relationships for CPN development. Comprehensive design rules that guide the production of CPNs with optimized performance are still lacking, hindering the systematic advancement of this field. Addressing this gap, we synthesized a series of new donor−acceptor (D−A) conjugated polymers (CPs), each incorporating a common acceptor unit paired with three distinct donor groups to assess their impact on optical and biological properties. The resulting nanoparticles exhibited excellent characteristics as fluorescent contrast agents, including enhanced fluorescence intensity in aqueous media along with favorable photostability. Studies using human colorectal carcinoma (HCT-116) and human umbilical vein endothelial cells (HUVEC) confirmed the CPNs' nontoxic nature, strong fluorescence, and biocompatibility. Notably, this study is the first to investigate the cellular uptake mechanism of CPNs in HCT-116 cells, offering valuable insights into their biological interactions. These findings not only demonstrate the potential of these newly developed CPNs for fluorescence imaging of HCT-116 but also underscore the urgent need for rational design frameworks to guide the future development of next-generation CPNs.

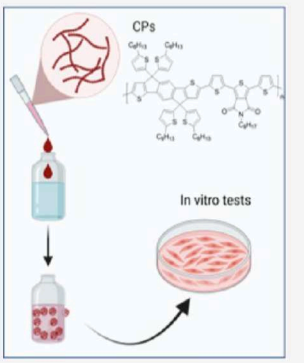

1. INTRODUCTION

Early detection of cancerous tumors is a cornerstone of effective treatment, as it significantly improves the chances of successful intervention and long-term survival. Despite advances in imaging technologies, a major barrier remains: the lack of highly specific and efficient optical contrast agents capable of distinguishing malignant from healthy tissues at the early stages of tumor development. Conventional optical contrast agents often exhibit poor photostability, limited brightness in biological environments, and nonspecific accumulation, which compromises imaging resolution and diagnostic accuracy.[1] This challenge is particularly evident in the detection of heterogeneous tumors, where generalized imaging tools fail to account for the molecular and cellular diversity across different cancer types and subtypes.[2]

CPNs synthesized from π-conjugated semiconducting polymers represent a promising platform for addressing these limitations due to their unique optical properties, such as strong absorption in the near-infrared (NIR) to shortwave infrared (SWIR) range, tunable fluorescence emission with high fluorescence quantum yields (QY), excellent photostability, and efficient nonradiative decay that make them excellent candidates for photoacoustic imaging, fluorescence-guided surgery, and photothermal therapy (PTT).[3−6]

To move beyond generalized applications, our primary focus is the rational design of specific CPNs tailored for human colorectal carcinoma (HCT-116) cells as an initial biological model. Then, as a next step, we aim to develop targeted, biocompatible CPNs that act as highly effective fluorescent contrast agents. This approach not only enables the exploration of structure−function relationships in polymer design but also sets the stage for creating precision imaging tools that can facilitate the early, accurate, and subtype-specific diagnosis of colorectal tumors in the future. However, until now, only a limited number (seven) of CPNs have been evaluated in different colorectal cancer cell lines (Figure 1).

One well-characterized system is based on PCPDTBSe, a low-bandgap D−A polymer originally developed for photovoltaics, which displays strong NIR absorption (≈750−800 nm) and efficient photothermal conversion.[7] While PCPDTBSe is nonfluorescent, hybrid nanoparticles, termed H-DAPPs, can be formed by blending with fluorescent CPs such as

Received: July 3, 2025
Revised: January 5, 2026
Accepted: January 7, 2026
Published: January 21, 2026

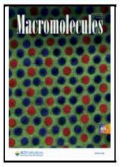

https://doi.org/10.1021/acs.macromol.5c01788
Macromolecules 2026, 59, 1429−1442

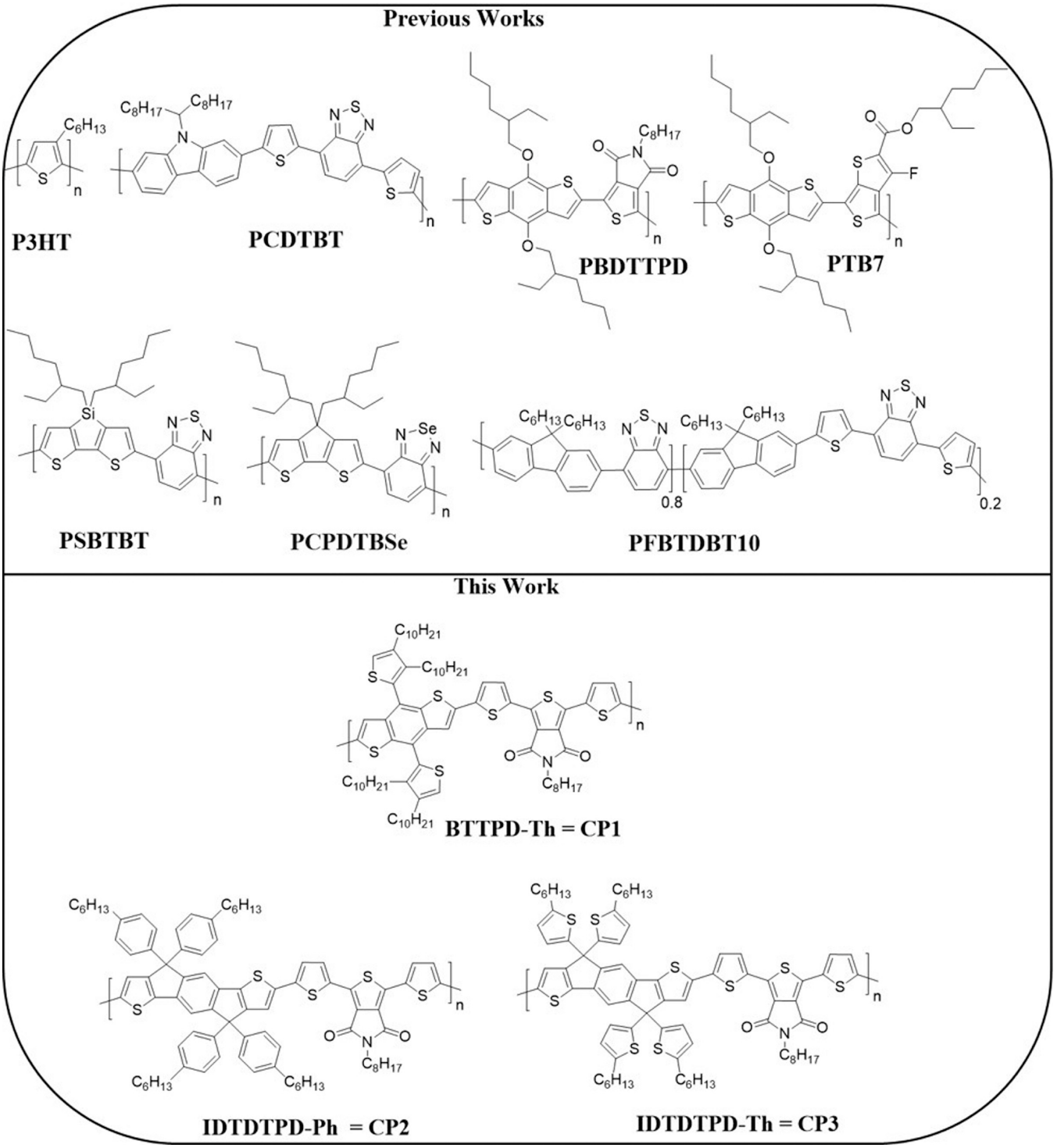

Figure 1. Chemical structures of the CPs used up to now as nanoparticles in colorectal cell lines (top) and the CPs developed in this work (bottom).

Table 1. Molecular Characteristics and Optical Properties of the Synthesized CPs

CPs	$\bar{M}_n$ (g/mol)	$\bar{M}_w$ (g/mol)	$Đ$	Absorption λ_{max}^{THF} (nm)	Emission λ_{max}^{THF} (nm)	QY (%)
CP1	70,500	197,000	2.80	590.0	683.0, 728.0	31.93 ± 1.6
CP2	156,000	444,000	2.85	579.0	697.0	36.27 ± 0.3
CP3	84,000	144,000	1.71	571.0	692.0	42.75 ± 1.4

PFBTDBT10, allowing for dual functionality in both imaging and therapy.[8,9] These hybrid formulations (commonly 95:5 PFBTDBT10:PCPDTBSe) have demonstrated significant efficacy in colorectal cell lines (e.g., HCT 116, CT26), in both 2D cultures and 3D tumor organoid models.[9] Targeting specificity has been improved through surface functionalization,

https://doi.org/10.1021/acs.macromol.5c01788
Macromolecules 2026, 59, 1429−1442

particularly with hyaluronic acid (HA),[8] which binds to CD44 receptors commonly overexpressed in colorectal tumors.[8] HA-coated H-DAPPs (HA-HDAPPs) show enhanced cellular uptake, improved biodistribution, and more effective photothermal ablation compared to nontargeted counterparts in xenograft and intraperitoneal models.

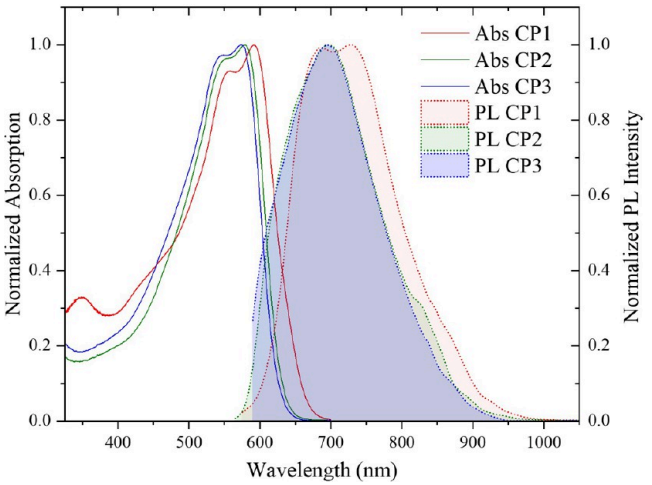

Figure 2. UV−vis and photoluminescence spectra of CP1, CP2, and CP3 diluted in THF.

Beyond PCPDTBSe-based systems, additional CPs have been investigated for their NIR/SWIR optical properties. These include polymers such as PCDTBT, PTB7, PSBTBT, PBDTTPD, and TQs, many of which exhibit emission beyond 700 nm.[10−13] Among them, PCDTBT nanoparticles have shown high QY (up to 7.18%) and efficient cellular uptake, including in macrophages and HCT 116 colorectal cancer cells. In preclinical assays, these nanoparticles generate sufficient heat under NIR laser excitation to induce >50% cell death through several millimeters of tissue-mimicking phantoms. Moreover, their strong absorption and emission profiles make them promising for emerging photoacoustic imaging platforms, though clinical applications in SWIR-guided colorectal imaging remain at the preclinical stage.

In this study, we developed a series of fluorescent contrast agents based on three rationally designed D−A CPs, one of which demonstrated a record-high QY (>9%) in the NIR region (≈700 nm) when formulated as aqueous nanoparticles. The CPs were synthesized using thienyl-substituted benzodithiophene (BDT) and either tetraphenyl- or tetrathienyl-substituted indacenodithiophene (IDT) derivatives as electron-donating units, paired with a dithieno-thienopyrroledione derivative as the electron-accepting unit. These polymers were converted into their corresponding aqueous CPNs via nanoprecipitation.[10] Comprehensive *in vitro* evaluations using HCT-116 colon cancer cells and HUVEC endothelial cells confirmed the potential of these CPNs as NIR fluorescent contrast agents,

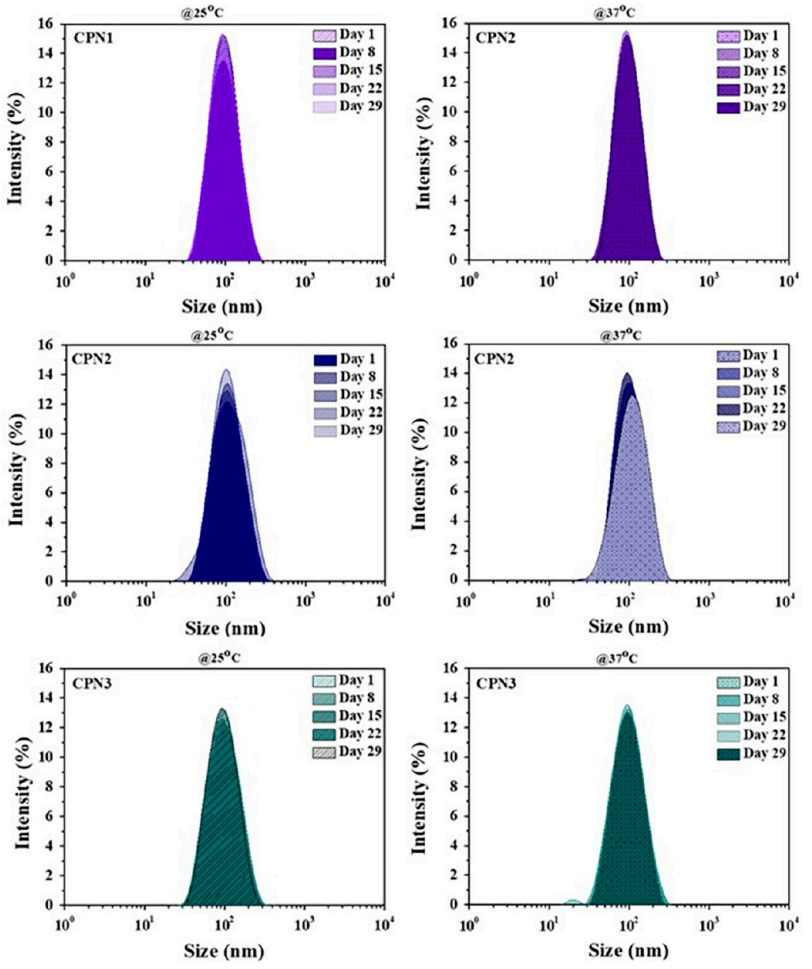

Figure 3. DLS diagrams at 25 and 37 °C for CPN1, CPN2, and CPN3 measured every 7 days for stability.

https://doi.org/10.1021/acs.macromol.5c01788
Macromolecules 2026, 59, 1429−1442

Table 2. Structural and Morphological Characteristics of Nanoprecipitated CPNs

	25 °C			37 °C			
CPNs	Z-Ave	PDI	PK1 mean	Z-Ave	PDI	PK1 mean	ζ (mV)
CPN1	90.92 ± 0.07	0.106 ± 0.001	103.13 ± 0.033	90.98 ± 0.17	0.115 ± 0.01	103.13 ± 1.04	−26.5
CPN2	96.06 ± 0.58	0.146 ± 0.005	114.03 ± 1.67	97.14 ± 0.52	0.141 ± 0.005	113.77 ± 1.2	−34.0
CPN3	86.46 ± 0.12	0.145 ± 0.007	102.7 ± 0.95	87.64 ± 0.26	0.156 ± 0003	105.4 ± 0.23	−25.7

Table 3. Optical Properties of Nanoprecipitated CPNs

CPNs	Absorption $\lambda_{max}H_2O$ (nm)	Emission $\lambda_{max}H_2O$ (nm)	QY (%)
CPN1	560	754	3.54 ± 0.33
CPN2	544	695	9.20 ± 0.21
CPN3	540	691	3.47 ± 0.20

and their cellular internalization mechanisms were systematically investigated.

2. MATERIALS AND METHODS

2.1. Synthesis of CPs

All reactions are air- and light-sensitive and, therefore, were performed under argon and in the dark. All glassware was washed using detergent (Teepol), rinsed with excess water, acetone, and methylene dichloride, and dried in an oven at 120 °C. All solvents and reagents were purchased from Sigma-Aldrich. Toluene was distilled using calcium hydride (CaH_2) and benzophenone prior to polymerization. For the synthesis, the monomer 1,3-bis(5-bromothiophen-2-yl)-5-octyl-4H-thieno[3,4-*c*]pyrrole-4,6(5H)-dione (Sigma-Aldrich) was combined with (4,8-bis(3,4-didecylthiophen-2-yl)benzo[1,2-b:4,5-b′]-dithiophene-2,6-diyl)bis(trimethylstannane) or 4,4,9,9-tetrakis(4-hexylphenyl)-4,9-dihydro-s-indaceno[1,2-b:5,6-b′]dithiophene-2,7-diyl)-bis(trimethylstannane) (Sigma-Aldrich) or (dimethyl(4,4,9,9-tetrakis-(5-hexylthiophen-2-yl)-7-(trimethylstannyl)-4,9-dihydro-s-indaceno-[1,2-b:5,6-b′]dithiophen-2-yl)stannyl)methylium (Sigma-Aldrich), to generate BTTPD-Th (CP1), IDTDTPD-Ph (CP2), and IDTDTPD-Th (CP3), respectively. Tris(dibenzylideneacetone)dipalladium(0) (Sigma-Aldrich) and tri(o-tolyl)phosphine (Sigma-Aldrich) were used as catalyst and ligand, and the polymerization took place in anhydrous toluene (Sigma-Aldrich). The polymerization reaction took place under 120 °C in an argon atmosphere for 24 h. Afterward, it was precipitated in methanol and collected for further purification. The final polymer was purified and fractionated via a sequential Soxhlet extraction with methanol, acetone, hexane, and chloroform.

2.2. Synthesis of CPNs

CPNs were prepared by using the nanoprecipitation method. Initially, each CP was dissolved separately in tetrahydrofuran (THF) at a concentration of 0.1 mg·mL^{-1}. THF is a low-boiling-point, aprotic, polar solvent that is miscible with water. At this low concentration, the polymer chains typically adopt an extended conformation. For nanoprecipitation, 7 mL of deionized water was placed under direct sonication by using a probe sonicator. While the polymer solution was sonicated, each polymer solution in THF was added dropwise into the water. The sonication facilitated rapid dispersion and nanoparticle formation, as the hydrophobic polymer chains aggregated in the aqueous environment. After addition, the solutions were left undisturbed overnight to allow complete evaporation of THF. Following solvent removal, stable aqueous CPNs were obtained. The nanoprecipitated CPNs were then characterized by dynamic light scattering (DLS), zeta potential analysis, UV−Vis absorption spectroscopy, fluorescence spectroscopy, and atomic force microscopy (AFM).

2.3. Characterization of Synthesized CPs and CPNs

2.3.1. Nuclear Magnetic Resonance (NMR). ^{1}H NMR measurements were carried out in solutions (1% w/v) of the copolymers using $CDCl_3$ (Acros 99.6%) as the solvent and tetramethylsilane (TMS) as the integral standard on a Bruker 400 MHz NMR spectrometer at ambient temperature. ^{13}C NMR spectra were acquired at the Bruker Avance 400 MHz spectrometer at a ^{13}C frequency of 62.90 MHz.

2.3.2. Gel Permeation Chromatography (GPC). The average molecular weights per number ($\bar{M}_n$) and dispersity ($Đ$) of the 1,2-Dichlorobenzene-soluble fractions of the CP1−3 were measured by high-temperature gel permeation chromatography (HT-GPC) at 150 °C based on monodispersed polystyrene standards. The gel permeation chromatograph used was a PL-GPC 220 High Temperature Chromatograph (Agilent Technologies).

2.3.3. Dynamic Light Scattering (DLS). Structural studies were performed using dynamic light scattering (DLS) to determine the mean diameter (d, nm) of nanodroplets and the polydispersity index (PDI) of the system. DLS measurements were performed using the Zetasizer Nano ZS device (ZEN3600, Malvern Instruments, UK) equipped with a He−Ne (632.8 nm) laser, and detection was performed at a scattering angle of 173°. The mean diameter of the dispersed nanodroplets was calculated by the Stokes−Einstein law:

$$R_H = \frac{k_B T}{6\pi\eta D}$$

where R_H is the hydrodynamic radii of nanodroplets, k_B is the Boltzmann constant, T is the absolute temperature, η is the viscosity of microemulsion (in specific temperature), and D is the diffusion constant, respectively.

After their preparation, the microemulsions were placed in a suitable glass cell in dust-free conditions. The experimental data were processed using version 6.32 of the Malvern Zetasizer Nano software (Malvern Panalytical Ltd., UK). The temperature during the measurements was constant at 25 or 37 °C. Experiments were performed in triplicate for each sample, and results are presented as average ± SD.

2.3.4. Absorption and Fluorescence Measurements. Absorption spectra were measured using a UV−vis Analytik Jena AG Germany Specord 205 spectrophotometer using a 1 cm path length quartz cuvette. The fluorescence emission spectra were recorded with an FS5 Spectrofluorometer (Edinburgh Instruments Ltd.). The samples were placed into 10 × 10 mm^2 Suprasil quartz cells with a septum cap, and the solutions were purged with argon for at least 10 min before the measurements. The relative fluorescence QY was determined using a dilute fluorenone solution in acetonitrile as the reference standard (Φ_r = 0.032)[14] and an excitation wavelength of 385 nm. The absorbance of all the solutions was 0.05−0.2 at the corresponding excitation wavelength.[15] Three measurements were performed for each solution. The excitation and emission slits were maintained unchanged during the emission experiments. The result is an average QY of the three measurements ± the standard deviation. The fluorescence QY has been calculated from the below equation:[16]

$$\Phi_x = \Phi_r(F_x/F_r)\cdot(A_r/A_x)\cdot(n^2{}_x/n^2{}_r)$$

where Φ_x is the photoluminescence QY of the unknown sample,
F is the area of the integration of the emission intensities,
n is the refractive index of the sample and the reference, and
A is the solution optical density at the excitation wavelength.
The indexes "r" and "x" refer to the reference and the unknown sample, respectively.

2.3.5. Atomic Force Microscopy (AFM). Atomic force microscopy (AFM) images were collected in tapping mode with a Bruker Multimode 3D Nanoscope using a microfabricated silicon cantilever type TAP-300G, with a tip radius of <10 nm and a force constant of approximately 20−75 N m^{-1}. The measured films were deposited on silicon substrates (Si wafers) by drop casting, and the measurement was

https://doi.org/10.1021/acs.macromol.5c01788
Macromolecules 2026, 59, 1429−1442

performed on the trace of the drop after using an ultrasonic water bath for 20 min.

2.3.6. Theoretical Calculations. The theoretical studies and calculations on the representative unit of the corresponding polymers in the present work are performed with the Gaussian 09 software package.[17] More specifically, instead of long aliphatic chains, the $-CH_3$ group was placed.

Initially, a preliminary landscape minimization study was performed through rapid scanning to find possible structures with semiempirical calculations (PM6), and then the minimized structures found were further minimized by DFT calculations using the B3LYP exchange-correlation functional[18] using the 6-31G(d) basis sets.[19] Vertical simulation energies of the singlet excited state were calculated using the time-dependent (TD-DFT) method at the B3LYP/6-31+G(d), PBE0 (PBE1PBE)/6-31+G(d), and CAM-B3LYP/6-31+G(d) levels, as well as with ZINDO calculations, which were performed to rule on the UV−vis spectra.

Finally, Physical Orbital or NBO calculations were performed to find the NBO charges, the bond order, and the corresponding molecular orbitals (MOs), as well as the interactions with nonbonding orbitals and the D−A electron interactions.

2.4. Cell Lines and Culture

The two cell lines used for the *in vitro* experiments were HCT-116 (human colon cancer)[20] and human umbilical vein endothelial cells (HUVECs).[21−23] HCT-116 cells were maintained in DMEM (PAN-Biotech) containing 4.5 g/L D-glucose, 10% FBS (Gibco), and 1% Penicillin/Streptomycin (Gibco) at 37 °C and 5% CO_2. HUVECs, p2-3, pooled from at least 3 donors, were plated on rat tail collagen (BD) and cultured in Medium 199 (Gibco) containing 20% heat-inactivated fetal calf serum, endothelial cell growth supplement (ECGS, 35 μg/mL), and 1% Penicillin/Streptomycin.[21] The cells were maintained in a humidified chamber with 5% CO_2 at 37 °C with media changes every 2−3 days until 80%−90% confluence. Cells were mycoplasma-free.

2.4.1. Cell Proliferation Assay. 10,000 HCT-116 and 7500 HUVECs were seeded in 96-well plates in the culture media described above. After overnight incubation, CPNs were added to the cells at the following concentrations: 0.5, 0.25, 0.125, 0.0625, 0.0325, and 0.0156 μg/mL. Cells were then placed into the IncuCyte Live Imaging System, and images were taken every 4 h for 72 h in total. To estimate cell proliferation, average cell surface area covered (%) was evaluated from triplicate wells, and the experiments were repeated at least three times.

2.4.2. Cell Uptake of CPNs. Cells were seeded onto coverslips in 24-well plates (HCT-116 or HUVECs, 70,000 cells/well) in the appropriate culture media at 37 °C for 24 h prior to addition of the CPNs. The medium was removed, and the cells were treated with medium containing 0.5 μg/mL of the CPNs for 24 h. After two washes with phosphate-buffered saline (PBS), the cells were fixed with 3.7% paraformaldehyde (PFA) for 10 min and washed twice with PBS, and then 50 mM NH_4Cl was added for 15 min. Samples were mounted in Mowiol and visualized by confocal microscopy (Confocal Leica SP5) using the 561 nm laser line. The objectives used were APO CS 40.0 × 1.25 OIL UV and APO CS 63.0 × 1.40 OIL UV. LasX and ImageJ software programs were used for image acquisition and analysis, respectively.

To perform the time course of CPN internalization into HCT-116 cells, CPNs were incubated with the cells for 15, 30, 45, 60, 90, 120, 240, and 360 min, and cells were then processed for confocal microscopy. To address the retention of CPNs in the cells, CPNs were added to the cells for 24 h, the medium was then removed, and the cells were washed extensively; fresh medium was added, and the cells were further incubated for 96 h total. Cells were then processed for confocal microscopy as above.

2.5. Antibodies and Chemicals

2.5.1. Immunofluorescence. Cells were seeded onto coverslips in 24-well plates (HCT-116, 70,000 cells/well) in the appropriate culture medium at 37 °C for 24 h prior to adding the CPNs. The medium was removed, and the cells were treated with medium containing 0.5 μg/mL of the nanoparticles for 24 h. After two washes with phosphate-buffered saline (PBS), the cells were fixed with methanol (MeOH) for 10 min at −20 °C, and indirect immunofluorescence followed as previously described.[24] The primary antibodies used were anti-LAMP1[25] and anti-CD63[26] (both from DSHB), and fluorescently labeled secondary antibodies were purchased from Jackson ImmunoResearch.

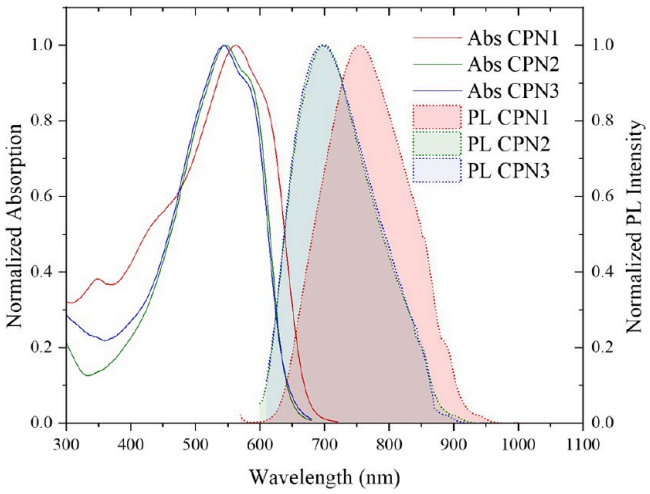

Figure 4. UV−vis and photoluminescence spectra of CPN1, CPN2, and CPN3 diluted in cell culture H_2O formed as nanoparticles by nanoprecipitation.

2.5.2. Lucifer Yellow Uptake. Lucifer Yellow (LY) was used to check the lysosomal integrity. HCT-116 cells were seeded (70,000 cells/well) in a 24-well plate on coverslips. LY was added at a concentration of 100 μg per milliliter in full medium, and cells were incubated for 24 h. After 24 h, the medium was removed, cells were washed three times, and fresh medium (no LY) was added to the cells. CPNs were added (0.5 μg/mL) to the cells and incubated for 24 h. As a positive control, cells were incubated in 100 μM chloroquine for 24 h in the absence of CPNs, and as a negative control, cells were incubated in the absence of CPNs and chloroquine. After 24 h, live confocal imaging was carried out to observe the LY and CPNs using a heated chamber at 37 °C and 5% CO_2. Leica SP5 was used, and the laser lines were 488 and 561 nm.

2.5.3. Dynasore Experiment. In a 24-well plate, HCT-116 cells (70,000 cells/well) were seeded on coverslips and serum-starved for 2 h. Dynasore was then added at a concentration of 150 μM along with the CPNs (0.5 μg/mL) for 6 and 8 h separately. Alexa488-Transferrin (Molecular Probes) 12.5 μg/mL was added for the last 10 min, and then the coverslips were fixed using 3.7% PFA and mounted using Mowiol-DABCO (both from Sigma). Samples were visualized by confocal microscopy using the laser lines 488 and 561 nm. LasX and ImageJ software programs were used for image acquisition and quantitation. HCT-116 cells were incubated with and without Dynasore for 6 and 8 h in the presence of CPNs.

2.5.4. siRNA Transfection of HCT-116. HCT-116 cells were cultured until they reached approximately 50% confluence and then transfected with siRNA targeting Clathrin Heavy Chain (CHC) (Ambion, AM16708A: 107566) at a final concentration of 50 nM, using Lipofectamine RNAiMAX reagent (Invitrogen). Two consecutive transfections were performed within a 24-h period, following the manufacturer's instructions. Forty-eight hours after the second transfection, the cells were serum-starved for 2 h, followed by a 6-h treatment with CPN3. Fifteen minutes prior to fixation, transferrin was added to the culture medium to assess the efficiency of CHC knockdown. Scrambled siRNA (Silencer Negative Control 5, Ambion) was used in parallel as a negative control in each transfection.

3. RESULTS AND DISCUSSION

3.1. Synthesis and Characterization of the Studied CPs

The D−A CPs comprised of thienyl-substituted BDT and tetraphenyl or tetrathienyl-substituted IDT derivatives as the

https://doi.org/10.1021/acs.macromol.5c01788
Macromolecules 2026, 59, 1429−1442

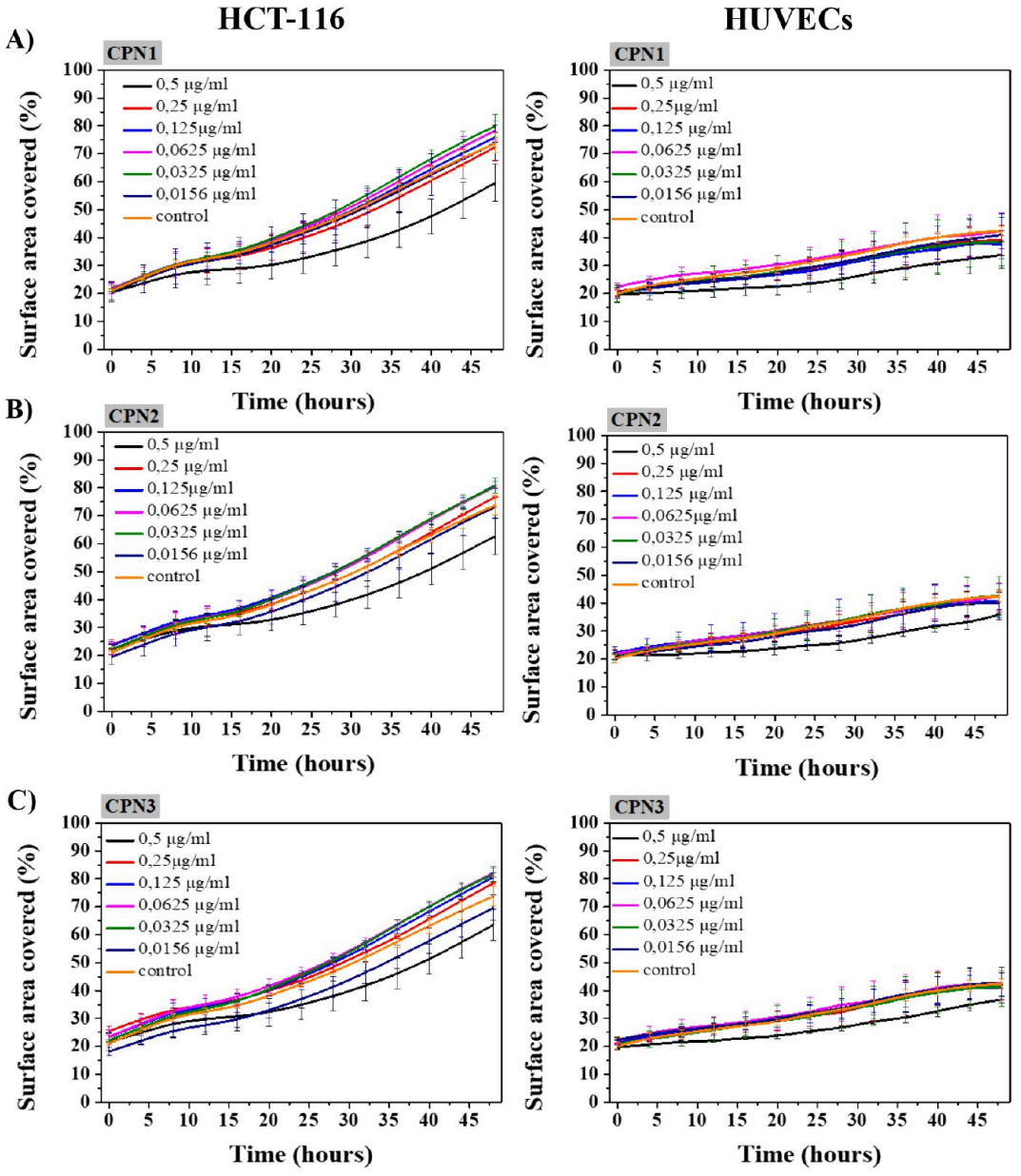

Figure 5. Cell proliferation of HCT-116 and HUVECs in the presence of CPNs. Graphs of cell surface area covered (%) vs time analyzed by IncuCyte for HCT-116 (left) and HUVEC cells (right) incubated for 48 h with (A) CPN1, (B) CPN2, and (C) CPN3. The graphs represent data from three experiments.

electron-donating units and dithieno-thienopyrroledione as the electron-withdrawing unit (mentioned as BTTPD-Th or **CP1** for simplicity, IDTDTPD-Ph or **CP2**, and IDTDTPD-Th or **CP3,** respectively) synthesized by palladium-catalyzed Stille cross-coupling polycondensation reactions and characterized thoroughly. The ^{1}H and ^{13}C NMR spectra are presented in the Supporting Information S2−S7. The average molecular weights per number ($\bar{M}_n$), per weight ($\bar{M}_w$), and dispersity ($Đ$) of the chloroform-soluble fractions of CP1, CP2, and CP3 were determined by high-temperature gel permeation chromatography (HT-GPC) using monodisperse polystyrene standards and summarized in Table 1 and illustrated in Figure S8. Notably, Soxhlet extraction left no insoluble residues, confirming the good solubility in chloroform and the effective purification of the polymers. All polymers exhibit very high $\bar{M}_w$ > 100 kD and reasonable $Đ$ (max 2.85 for CP1 and CP2). Although CP2 and CP3 share an identical conjugated backbone, their different side groups (phenyl in CP2 and thiophene in CP3) significantly influence their average molecular weight characteristics and dispersity.

The optical properties of the polymers were recorded by UV−vis absorption and photoluminescence (Figure 2) in a THF solution. All polymers demonstrated absorption in the 400−650 nm range and fluorescence emission spanning the visible to NIR region (600−950 nm), which are beneficial for bioimaging applications. Among the three, CP3 displayed the highest photoluminescence QY in THF solution (Table 1), indicating that the bonding of the two thiophene rings to the central phenyl ring by two 5-member bridged sites in IDT enhances the emission QY versus the polycyclic BDT, where the two thiophenes are fused on the central phenyl ring. Moreover, between CP2 and CP3, it is not clear if the lower molecular

https://doi.org/10.1021/acs.macromol.5c01788
Macromolecules 2026, 59, 1429−1442

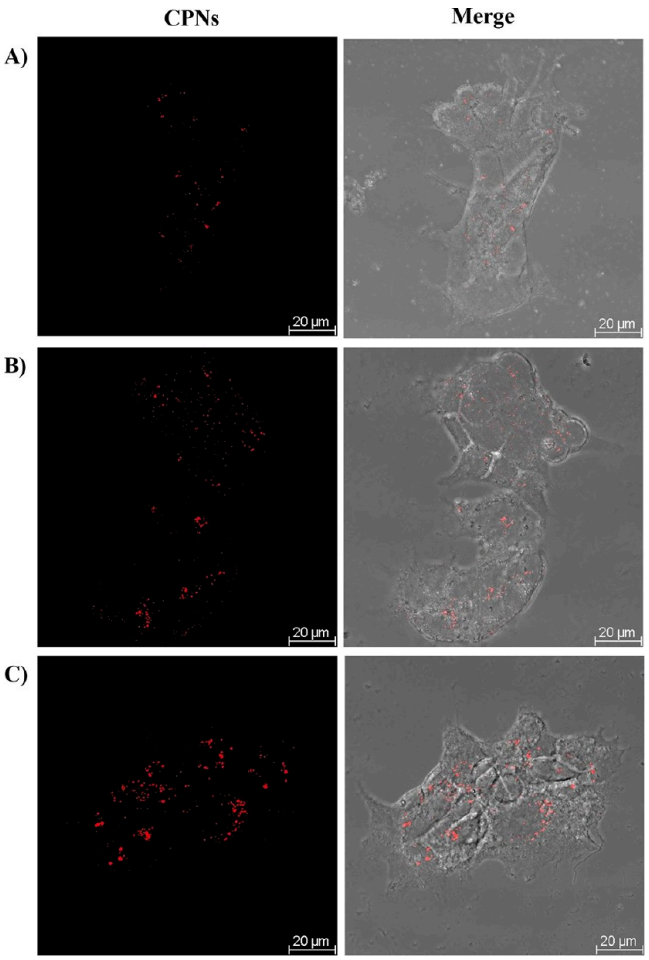

Figure 6. HCT-116 cells were incubated with 0.5 μg/mL of (A) CPN1, (B) CPN2, and (C) CPN3 for 24 h and processed for confocal microscopy (n = 3). Representative maximum projections and BF are presented. Scale bar: 20 μm.

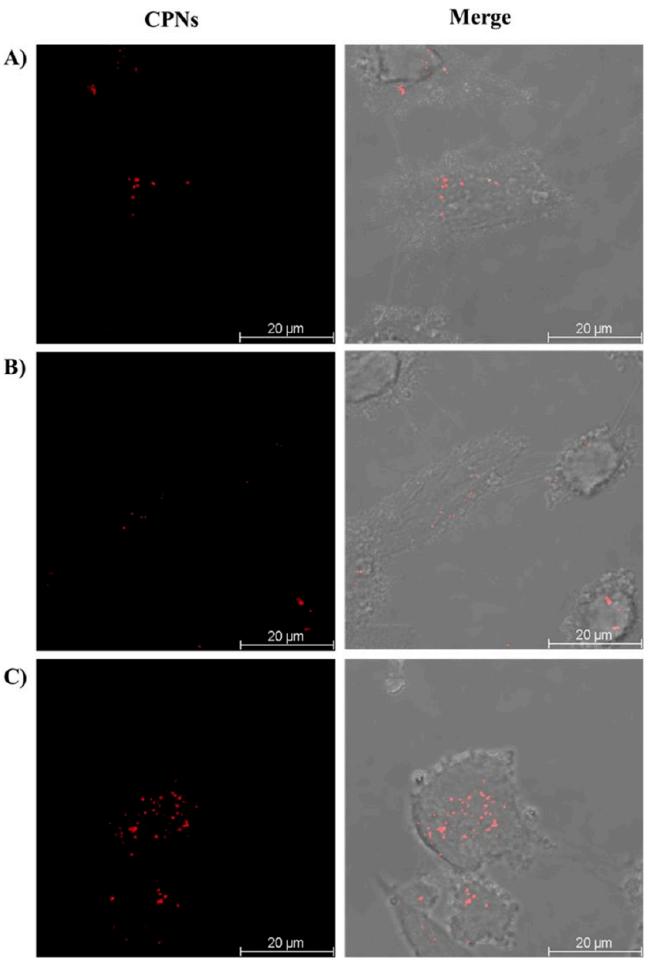

Figure 7. HUVECs were incubated with 0.5 μg/mL of (A) CPN1, (B) CPN2, and (C) CPN3 for 24 h and processed for confocal microscopy (n = 2). Representative maximum projections and BF are presented. Scale bar: 20 μm.

weight characteristics or the type of side groups (phenyl versus thienyl) affect primary emission QY.

The depiction of the theoretical molecular orbitals can provide more information about the transfer of electrons, which is shown in Supporting Information S8. In addition, the theoretical calculations predicted almost precisely the λ_{max} with an error of ≈20 nm, which is logical since we calculated for one structural unit instead of the many that a polymer has. Moreover, the NBO method showed D−A properties and localization of the electrons. This led us to determine that this theoretical tool can be used for future designing of other structures.

3.2. Preparation and Characterization of CPNs

In this work, the CPNs is taking place through the nanoprecipitation method. For the formation of the CPNs via the nanoprecipitation method, first, each CP was dissolved in THF, which is a low-boiling-point aprotic polar solvent miscible with the water at a concentration of 0.1 mg mL^{-1}. At such a low concentration, the polymer chains usually adopt their extended form. Then, each different polymer solution was added dropwise to 7 mL of deionized water, followed by sonication at room temperature. The solutions were left overnight to allow complete evaporation of the THF. After this procedure, stable aqueous CPNs are formed through aggregate formation of the hydrophobic conjugated polymer chains with a concentration of 1.7 ppm.

It is important to use different characterization techniques to calculate the size and distribution of the prepared nanoparticles to obtain a more complete view of the CPNs and their behavior. To evaluate the sizes of the formatted aqueous CPNs, dynamic light scattering (DLS) measurements were performed at room temperature 25 °C a day after their preparation (Figure 3), and the results are depicted in Table 2. The DLS measurements indicate that the aqueous nanoparticles exhibit a unimodal size distribution. The majority of the CPNs revealed a hydrodynamic diameter between 70 and 110 nm (Table 2). On one hand, smaller nanoparticles (<50 nm) may facilitate more efficient tissue penetration and intracellular uptake, potentially improving therapeutic delivery. On the other hand, excessively small sizes can increase the risk of rapid clearance from circulation, reduced loading capacity, and higher surface reactivity, which may raise concerns regarding stability and safety. Thus, while smaller nanoparticles may indeed offer advantages in some contexts, an optimal size must balance absorption, circulation half-life, stability, and the intended biological application. Accordingly, we emphasize that while the 80−100 nm range represents the practical outcome of our current fabrication method, future studies employing microfluidic or other

https://doi.org/10.1021/acs.macromol.5c01788
Macromolecules 2026, 59, 1429−1442

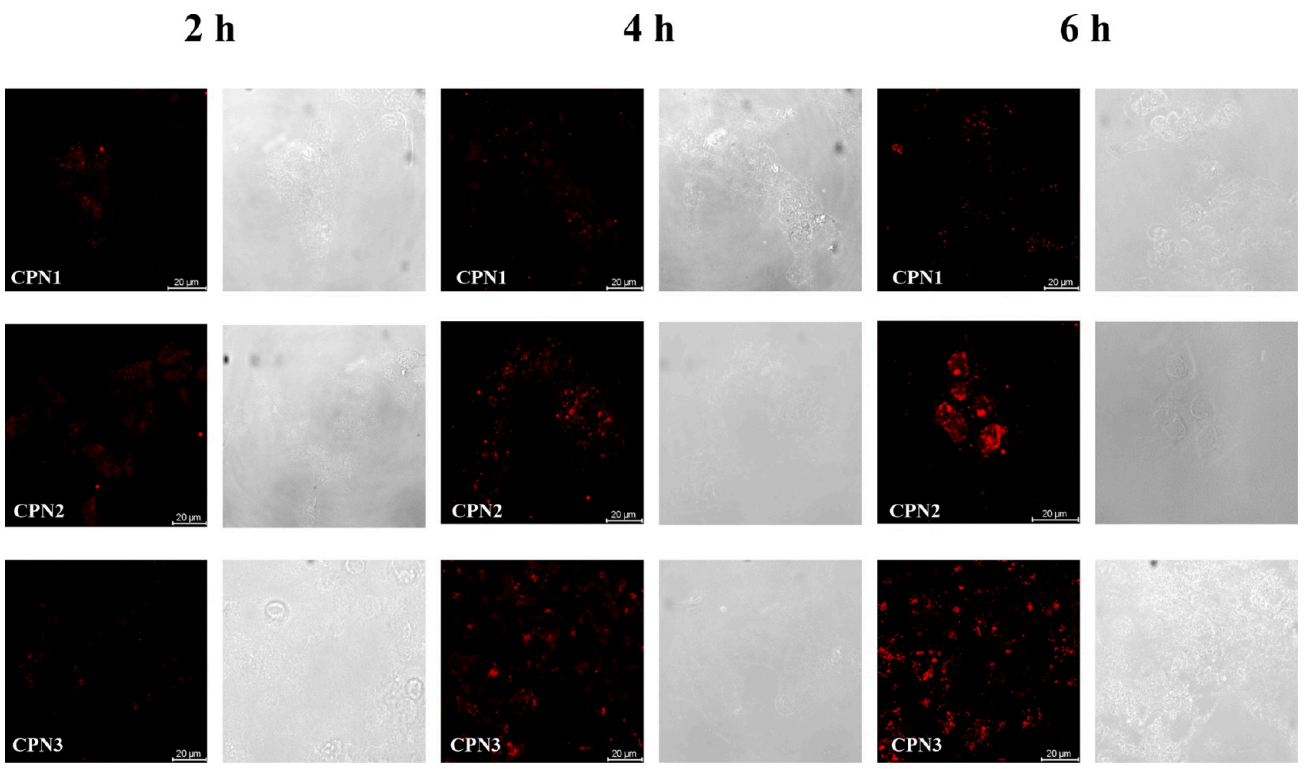

Figure 8. Confocal fluorescence microscopy images in maximum projection pictures from 2, 4, and 6 h incubation of studied CPNs in HCT-116 cells examining the time point of their internalization. Representative images after confocal microscopy are presented (n = 2). Scale bar: 20 μm.

advanced synthesis techniques could allow exploration of smaller sizes and their biological performance.

Simultaneously with the DLS measurements, the zeta potential of the CPNs was measured. The colloidal stability of our aqueous CPNs is confirmed by the substantial and negative zeta potential, as shown in Table 2. It is obvious that the nanoparticles display highly negative zeta potential values ranging from −25.7 to −34 mV. When studying CPNs for their possible use as contrast agents or nanocarriers, it is important to study their size and stability over a period of time at two temperatures, which are room and body temperature (25/37 °C). Figure 3 shows the DLS diagrams over a 30-day period. The CPNs' size remains stable with fluctuations of 1−3 nm. The average size in nm on day 1 of this specific batch of the CPN1 was 90.92 ± 0.07 and 90.98 ± 0.17 for 25 and 37 °C, respectively, followed by the CPN2 size with values of 96.06 ± 0.58 and 97.14 ± 0.52 at 25 and 37 °C, respectively, and the CPN3 size at 86.46 ± 0.12 and 87.64 ± 0.26 at 25 and 37 °C, respectively. Moreover, AFM (Figure S10) was performed to determine the shape of the CPNs after their dehydration on a silicon surface and to compare the size measurements to those in aqueous solution. We found an almost round (oval) shape, and the sizes of CPN1, CPN2, and CPN3 were determined to be 132.7, 125.9, and 95.67 nm, respectively, and were slightly larger than those observed from DLS.

The optical properties of CPN1−3 reveal distinct differences in their absorption, emission, and QY characteristics in aqueous environments (Table 3). All three CPNs exhibit absorption maxima (λ_{max}) in the visible range (Figure 4), with CPN1 absorbing at the longest wavelength (560 nm), followed by CPN2 (544 nm) and CPN3 (540 nm). The red-shifted absorption of CPN1 suggests a more extended π-conjugation or a stronger donor−acceptor (D−A) interaction within the nanoparticle microstructure compared to CPN2 and CPN3. The substitution pattern on the BDT unit appears to influence this behavior, where the thienyl-substituted BDT in CPN1 seems to allow for a slightly more planar conjugated system than CPN2 and CPN3, thereby enhancing conjugation length and red-shifting the absorption.

The emission maxima (λ_{em}) follow a similar trend, with CPN1 emitting at 754 nm, while CPN2 and CPN3 exhibit blue-shifted emissions at 695 and 691 nm, respectively (Figure 4). Still in the NIR, though. The large Stokes shift observed in CPN1 (194 nm) compared to CPN2 (151 nm) and CPN3 (151 nm) is indicative of significant reorganization energy or excitonic relaxation processes, potentially due to the structural rigidity in CPN1. Despite having the lowest emission wavelength, CPN2 exhibits the highest fluorescence QY at 9.2%, which is substantially greater than that of CPN1 (3.54%) and CPN3 (3.47%). This suggests that the balance between radiative and nonradiative decay processes in CPN2 is more favorable, likely due to reduced aggregation-induced quenching or enhanced solubility of the nanoparticle formulation. The high QY of CPN2 also indicates that its electronic configuration supports efficient exciton generation and emission. Overall, the optical data suggest that subtle changes in the side-chain structure of the donor unit significantly influence the photophysical behavior of the CPNs. CPN2 emerges as the most promising candidate for NIR fluorescence imaging applications due to its high emission efficiency (9.2%) and suitable NIR emission (≈700 nm).

3.3. In Vitro Results

Engineering nanoparticles for drug delivery offers significant potential to enhance cancer therapy. However, their effectiveness depends not only on successful cellular entry but also on whether they cause toxicity or membrane damage, their ability to accumulate within target cells, and the rate at which they are degraded or lost over time. To address these questions, we used

https://doi.org/10.1021/acs.macromol.5c01788
Macromolecules 2026, 59, 1429−1442

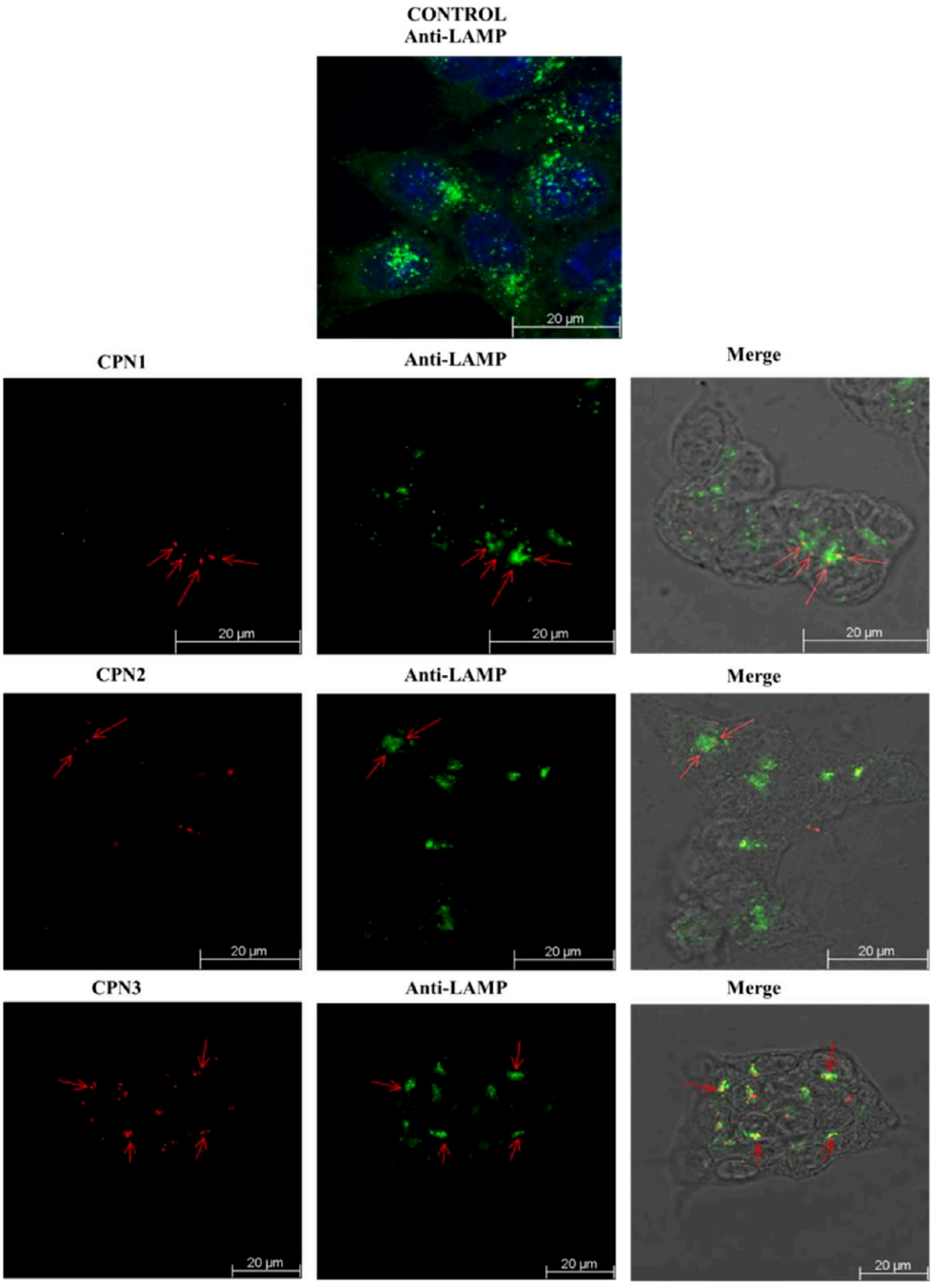

Figure 9. Confocal fluorescence microscopy images in maximum projection of HCT-116 cells after 24 h of incubation with the studied CPNs using the antibodies LAMP1. Representative images after confocal microscopy are presented (n = 2). Scale bar: 20 μm.

2 cell lines: a human colon cancer (HCT-116) and human primary umbilical vein endothelial cells (HUVECs). We first addressed whether the CPNs affected cell proliferation. CPNs did not alter cell proliferation in HCT-116 and HUVEC cells after their incubation for 48 h at the following concentrations: 0.25, 0.125, 0.0625, 0.0325, and 0.0156 μg/mL (Figure 5). At 0.5 μg/mL, however, there was an inhibition of cell proliferation of HCT-116 cells of approximately 10%, and this effect was also seen in HUVECs (Figures S11 and S12).

To address whether the CPNs were internalized in HCT-116 and HUVEC cells, the CPNs were added to the cells for 24 h at a concentration of 0.5 μg/mL. As shown in Figures 6 and 7, all three CPNs were internalized in both cell lines.

CPN1 was internalized; however, it had the lowest fluorescence signal of all CPNs tested (Figures 6A and 7A). CPN2 had the highest fluorescence signal in both cell lines, as this was expected since it had the highest QY; however, even though CPN2 was internalized, it also exhibited a tendency to accumulate at areas of cell−cell contact and around the plasma membrane (Figure S13). CPN3 had the highest number of internalized CPNs per cell and a good fluorescence signal (Figures 6C and 7C). The enhanced compatibility of CPN1 and CPN3 with the cell membrane may be attributed to the presence

https://doi.org/10.1021/acs.macromol.5c01788
Macromolecules 2026, 59, 1429−1442

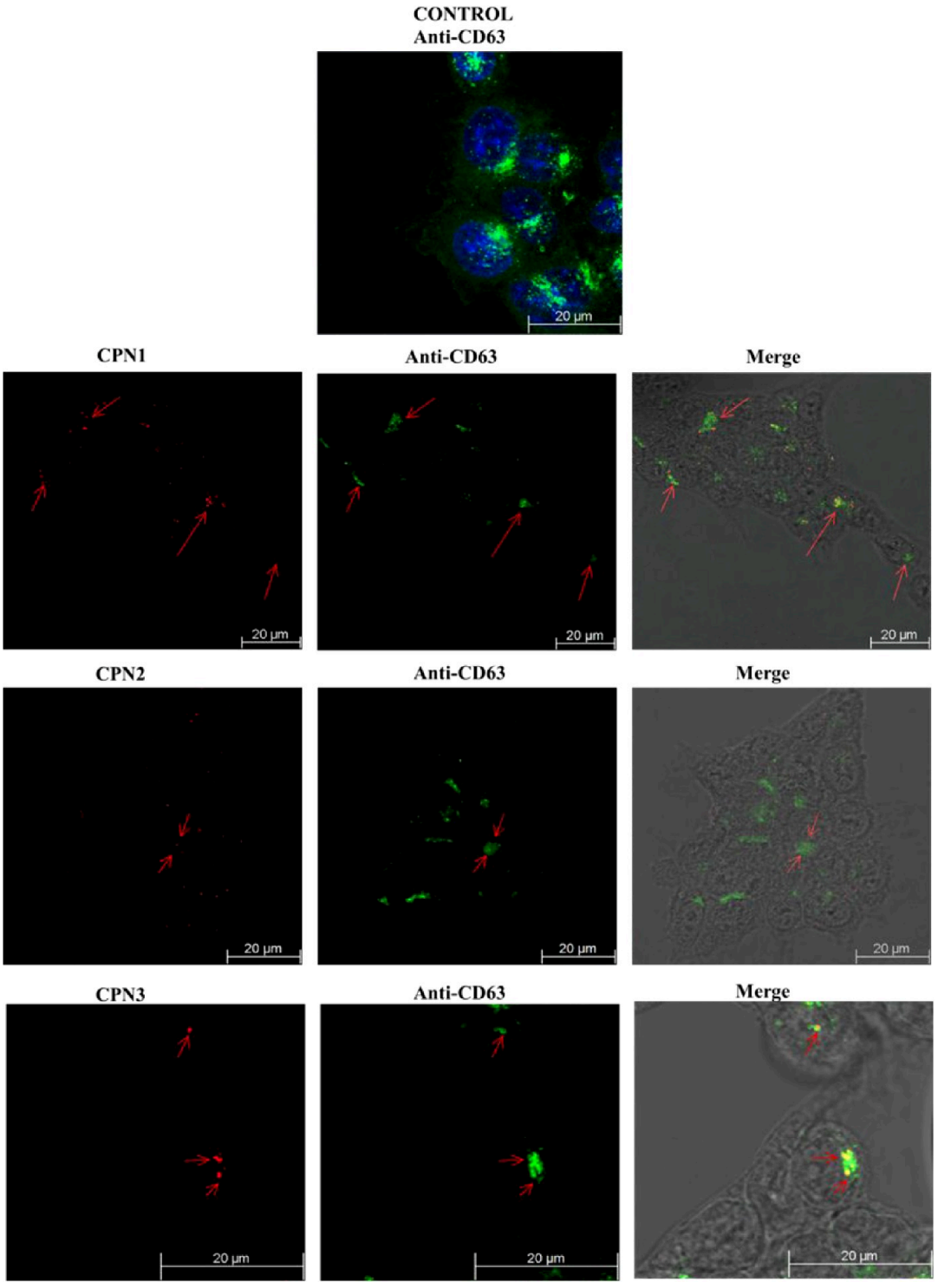

Figure 10. Confocal fluorescence microscopy images in maximum projection of HCT-116 cells after 24 h of incubation with the studied CPNs using the antibodies CD63. Representative images after confocal microscopy are presented (n = 2). Scale bar: 20 μm.

of thienyl side groups, which likely facilitate stronger biophysical interactions with membrane-associated biocomponents. This behavior appears to be independent of the core units (BDT or IDT) and is instead primarily influenced by the nature of the side chains, thienyl in CPN1 and CPN3 versus phenyl in CPN2. However, this hypothesis warrants further investigation to be fully confirmed.

We addressed the kinetics of internalization of the CPNs in HCT-116 cells. Internalization was visible at a low level from 2 h of incubation, peaking at 6 h (Figure 8).

We also addressed the intracellular localization of the CPNs after internalization for 24 h. The CPNs colocalized with LAMP and CD63 vesicular structures, suggesting accumulation of the CPNs in the late endosomal/lysosomal compartments (Figures 9 and 10, respectively).

https://doi.org/10.1021/acs.macromol.5c01788
Macromolecules 2026, 59, 1429−1442

In addition, we addressed whether the accumulation of CPNs in the lysosomal compartment led to lysosomal damage and leakage using Lucifer Yellow in living HCT-116 cells by confocal microscopy. As shown in the Supporting Information (video section), the lysosomes in all cases were unaffected by the accumulation of the CPNs.

To determine if the CPNs are cleared from the cells postuptake, CPNs were internalized in HCT-116 cells for 24 h, cells were washed to remove the CPNs that had not been uptaken, and the cells were left for 96 h and analyzed by confocal microscopy (Figure 11).

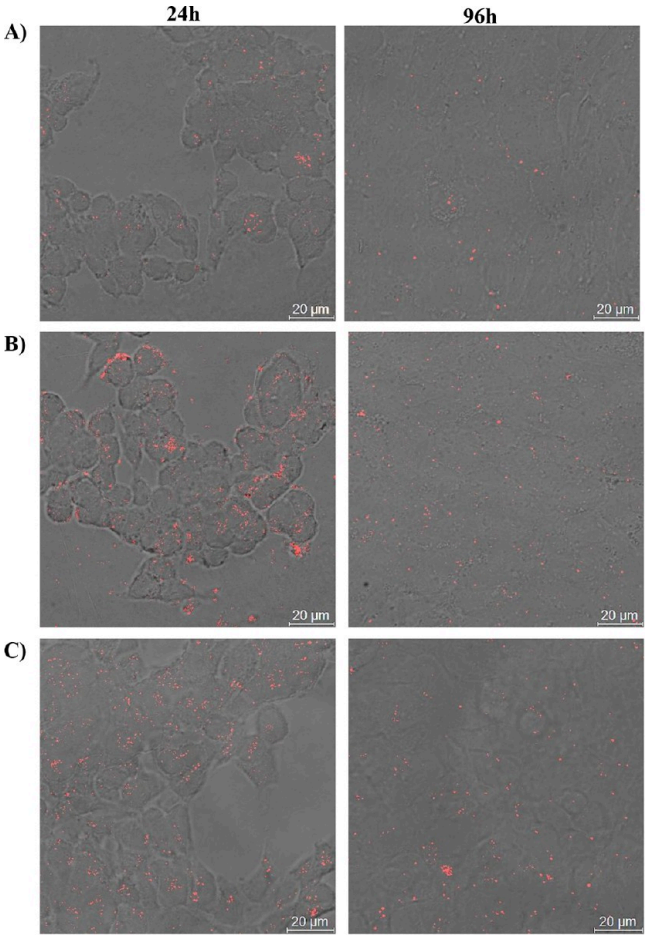

Figure 11. Confocal fluorescence microscopy images of (A) CPN1, (B) CPN2, and (C) CPN3 in maximum projection of HCT-116 cells with the studied CPNs after 24 h (left) and after 96 h (right). Representative images after confocal microscopy are presented (n = 1). Scale bar: 20 μm.

All three CPNs were still present inside the cells following 96 h of incubation, suggesting that the uptaken CPNs are retained in the lysosomal compartment; however, the amount of CPNs at 96 h is less than that at 24 h, suggesting that there is a loss of CPNs from the cells over this time period or dilution upon cell proliferation.

Having established that the CPNs are indeed internalized in both HCT-116 and HUVECs, we addressed the mechanism by which this occurs. The main route of internalization into the cell is via endocytosis, and the endocytic route is an important consideration and can affect the efficiency and specificity of the cellular uptake. There are many endocytic pathways, and clathrin-mediated endocytosis (CME) is the most well-characterized and constitutively active endocytic pathway. In addition to CME, multiple distinct forms of clathrin-independent endocytosis (CIE) have been identified. These include the CLIC/GEEC pathway (involving clathrin-independent carriers and GPI-anchored proteins), IL2Rβ uptake, EGFR nonclathrin endocytosis (EGFR-NCE), Fast Endophilin-Mediated Endocytosis (FEME), massive endocytosis (MEND), macropinocytosis, and neuron-specific mechanisms such as activity-dependent bulk endocytosis (ADBE) and ultrafast endocytosis (UFE).[27] The endocytic pathways mentioned above can be divided into dynamin-dependent and -independent. The dynamin-dependent pathways include CME, EGFR-NCE, IL2Rb, ADBE, UFE, and FEME, and the dynamin-independent pathways include CLIC/GEEC, MEND, and micropinocytosis.[27,28] However, endocytic mechanisms can vary across cell types, between *in vitro* and *in vivo* conditions, and depending on the size of the internalized cargo, making generalizations unreliable.[29]

In this study, we used dynasore, a small-molecule dynamin inhibitor, to investigate whether the internalization of CPN3 in HCT-116 cells is dynamin-dependent. Alexa488-Transferrin, which is internalized via the dynamin-dependent CME pathway, served as a positive control to confirm the effectiveness of dynasore inhibition. Our results demonstrate that dynasore significantly inhibited CPN3 internalization, suggesting that its uptake in HCT-116 cells is dynamin-dependent (Figures 12 and S14 showing the quantitation from three independent experiments).

CME, EGFR-NCE, IL2Rb, ADBE, UFE, and FEME are all dynamin-dependent endocytic pathways, and ADBE and UFE are neuron-specific, so CME, EGFR-NCE, IL2Rb, and FEME are possible pathways regulating CPN3 uptake. We addressed whether the pathway was CME by siRNA silencing of the clathrin heavy chain (CHC). Alexa488-Transferrin, which is internalized via the CME pathway, served as a positive control to confirm the effectiveness of siCHC silencing. In cells transfected with a scrambled siRNA control (Figure 13 scrambled siRNA), transferrin and CPN3 were endocytosed into HCT-116 cells. In cells transfected with siRNA CHC, transferrin internalization was inhibited, as expected (Figure 13); however, CPN3 was internalized. This result confirms that CPN3 internalization in HCT-116 cells is CME-independent. Further experiments are required to address whether the mechanism is EGFR-NCE, IL2Rb, or FEME, having first addressed which of these pathways is active in HCT-116 cells. Two consecutive transfections were performed within a 24-h period, following the manufacturer's instructions. Forty-eight hours (48 h) after the second transfection, the cells were serum-starved for 2 h, followed by a 6-h treatment with CPN3. Fifteen minutes prior to fixation, transferrin was added to the culture medium to assess the efficiency of CHC knockdown. Scrambled siRNA (Silencer Negative Control 5, Ambion) was used in parallel as a negative control in each transfection.

4. CONCLUSIONS

In this study, three newly synthesized D−A CPs were successfully characterized, all of which exhibit absorption in the UV−vis range and emission at the NIR. Using the nanoprecipitation method, the CPs were converted into water-dispersible CPNs, enhancing their suitability for biological applications, particularly with mammalian cells. The resulting CPNs remain stable for at least 1 month and exhibit uniform size

https://doi.org/10.1021/acs.macromol.5c01788
Macromolecules 2026, 59, 1429−1442

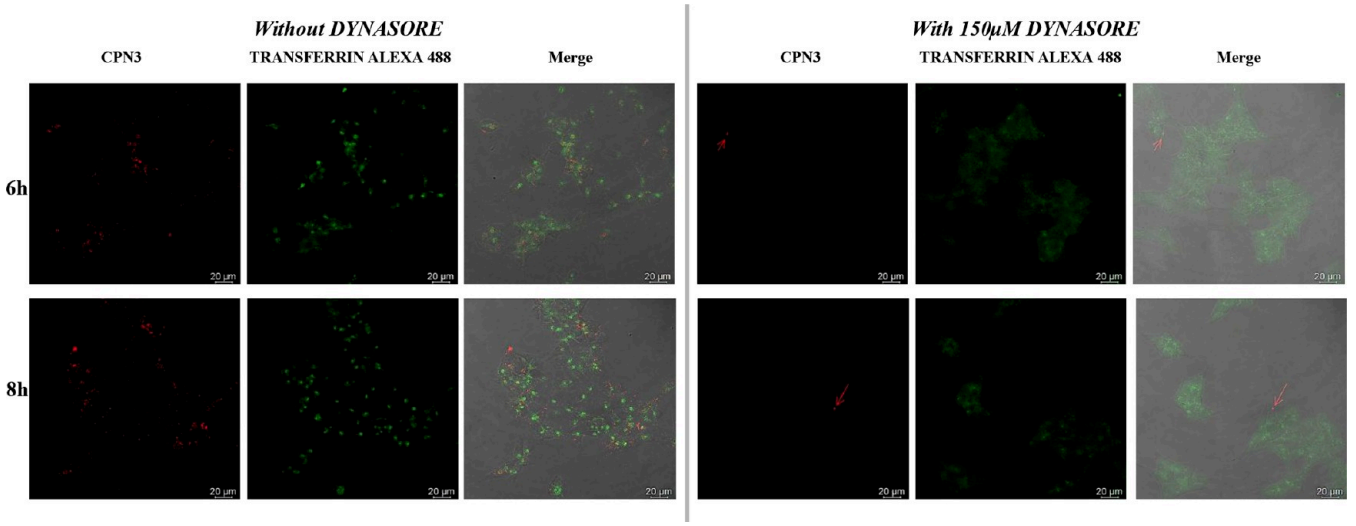

Figure 12. Confocal fluorescence microscopy images in maximum projection of HCT-116 cells with CPN3 with and without dynasore incubated for 6 and 8 h. Alexa488-Transferrin was internalized for the last 10 min. Representative images after confocal microscopy are presented ($n = 3$). Scale bar: 20 μm.

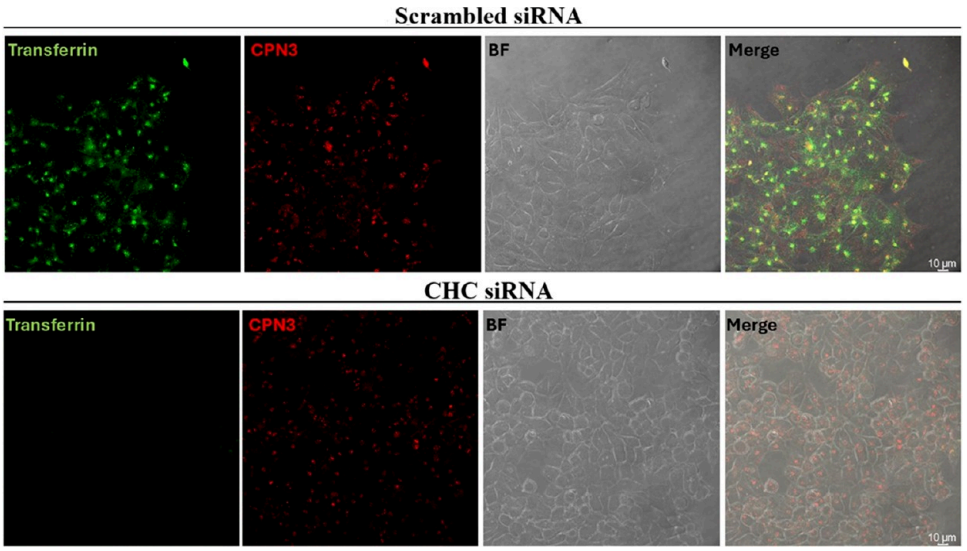

Figure 13. HCT cells were cultured on coverslips until 50% confluent. Then cells were transfected sequentially, with a 24-h gap, with either scrambled siRNA or siRNA for Clathrin Heavy Chain. Forty-eight hours after the second transfection, the cells were serum-starved for 2 h, followed by the addition of CPN3 for 6 h. Fifteen minutes prior to fixation, Alexa488-Transferrin was added to the culture medium to assess the efficiency of CHC knockdown. Following fixation, samples were mounted for Leica TCS-SP5 scanning confocal microscopy imaging, equipped with Argon/SS-561/HeNe lasers, APO CS 63.0 × 1.40 OIL UV objective lenses, and Leica Las AF Lite software.

distribution, with average diameters between 80−100 nm and low dispersity. Their optical behavior closely mirrors that of the parent CPs in THF, though with a lower QY (ranging from 3.5% to 9.2%). However, the 9.2% QY reported for CPN2 at ≈700 nm is the highest reported among all of the other CPNs utilized in colorectal cell lines.

In vitro evaluations demonstrated that the aqueous CPNs are nontoxic to both HCT-116 and HUVEC cells at concentrations up to 0.5 μg/mL. After 6 h of incubation, all CPNs were efficiently internalized by the cells, showing strong fluorescence signals and retention within HCT-116 cells for up to 96 h. Following 24 h of internalization, the CPNs localized predominantly in lysosomal and multivesicular compartments, without causing any detectable damage to the endocytic membranes. Internalization in HCT-116 cells was clathrin-independent and dynamin-dependent.

The findings of this study offer valuable new insights and design guidelines for the development of next-generation CPNs as fluorescent contrast agents, specifically for HCT-116 and HUVEC cell lines. The results highlight the critical influence of molecular structure, particularly the incorporation of IDT on the main chain versus BDT and the thienyl side groups versus phenyl, on the biological performance and optical properties of the CPNs. While thienyl-functionalized polymers exhibit a lower QY versus their phenyl analogue, they demonstrated enhanced cellular uptake and promising localization within endocytic compartments, without inducing cytotoxic effects. These findings indicate that incorporating thienyl groups into the polymer backbone should be a key focus in the design of future CPNs. However, to fully capitalize on this strategy, such structural modifications should also be optimized to enhance the

https://doi.org/10.1021/acs.macromol.5c01788
Macromolecules 2026, 59, 1429−1442

fluorescence QY in the NIR region, thereby improving their effectiveness for deep tissue imaging.

■ ASSOCIATED CONTENT

Supporting Information

The Supporting Information is available free of charge at https://pubs.acs.org/doi/10.1021/acs.macromol.5c01788.

Synthesis scheme of CP1, CP2, and CP3; ^{1}H NMR and ^{13}C NMR spectra of CP1, CP2, and CP3; GPC chromatographs of CP1, CP2, and CP3; energy levels orbital calculations by TD-DFT; AFM 3D morphology images of CPN1, CPN2, and CPN3; IncuCyte proliferation images of HCT-116 and HUVEC cells incubated with CPNs; confocal fluorescence microscopy images of CPN2 uptake in HCT-116 cells; quantification of CPN3 uptake with dynasore treatment for dynamin inhibition analysis (PDF)

The accumulation of CPNs in the lysosomal compartment using Lucifer Yellow in living HCT-116 cells by confocal microscopy (Video 1) (AVI)

Accumulation of CPNs in the lysosomal compartment (Video 2) (AVI)

Accumulation of CPNs in the lysosomal compartment (Video 3) (AVI)

■ AUTHOR INFORMATION

Corresponding Author

Christos L. Chochos − *Institute of Chemical Biology, National Hellenic Research Foundation, Athens 11635, Greece;* orcid.org/0000-0002-7783-157X; Email: chochos@eie.gr

Authors

Aristea Pavlou − *Institute of Chemical Biology, National Hellenic Research Foundation, Athens 11635, Greece; Biomedical Research Institute, Foundation for Research and Technology-Hellas (FORTH), University Campus of Ioannina, Ioannina 45110, Greece; Department of Chemistry, Section of Organic Chemistry and Biochemistry, University of Ioannina, Ioannina 45110, Greece;* orcid.org/0000-0001-5076-818X

Athanasios Katsouras − *Biomedical Research Institute, Foundation for Research and Technology-Hellas (FORTH), University Campus of Ioannina, Ioannina 45110, Greece; Department of Materials Science and Engineering, University of Ioannina, Ioannina 45110, Greece*

Maria Markou − *Biomedical Research Institute, Foundation for Research and Technology-Hellas (FORTH), University Campus of Ioannina, Ioannina 45110, Greece*

Alkmini Nega − *Institute of Chemical Biology, National Hellenic Research Foundation, Athens 11635, Greece; Clinical Cooperation Unit Nuclear Medicine, German Cancer Research Center (DKFZ), Heidelberg 69120, Germany*

Sofia Bellou − *Biomedical Research Institute, Foundation for Research and Technology-Hellas (FORTH), University Campus of Ioannina, Ioannina 45110, Greece*

Panagiota Koralli − *Institute of Chemical Biology, National Hellenic Research Foundation, Athens 11635, Greece*

Andriana Schiza − *Institute of Chemical Biology, National Hellenic Research Foundation, Athens 11635, Greece*

Nikolaos Chalmpes − *Department of Materials Science and Engineering, University of Ioannina, Ioannina 45110, Greece;* orcid.org/0000-0003-2744-5934

Vasilis G. Gregoriou − *Institute of Chemical Biology, National Hellenic Research Foundation, Athens 11635, Greece*

Antonia Dimitrakopoulou-Strauss − *Clinical Cooperation Unit Nuclear Medicine, German Cancer Research Center (DKFZ), Heidelberg 69120, Germany*

Theodore Fotsis − *Biomedical Research Institute, Foundation for Research and Technology-Hellas (FORTH), University Campus of Ioannina, Ioannina 45110, Greece*

Apostolos Avgeropoulos − *Department of Materials Science and Engineering, University of Ioannina, Ioannina 45110, Greece;* orcid.org/0000-0002-6203-9942

Michael G. Siskos − *Department of Chemistry, Section of Organic Chemistry and Biochemistry, University of Ioannina, Ioannina 45110, Greece*

Carol Murphy − *Biomedical Research Institute, Foundation for Research and Technology-Hellas (FORTH), University Campus of Ioannina, Ioannina 45110, Greece*

Complete contact information is available at: https://pubs.acs.org/10.1021/acs.macromol.5c01788

Funding

The open access publishing of this article is financially supported by HEAL-Link.

Notes

The authors declare no competing financial interest.

■ ACKNOWLEDGMENTS

C.L.C., V.G.G., A.D.-S., and A.N. would like to thank the Helmholtz European partnering program for the cooperation between the German Cancer Research Center (DKFZ) and the National Hellenic Research Foundation (NHRF) to build the Athens Comprehensive Cancer Center (ACCC) for the financial support. Moreover, C.L.C. acknowledges the Hellenic Foundation for Research and Innovation (H.F.R.I.) under the "2nd Call for H.F.R.I. Research Projects to support Faculty Members & Researchers" (Project Number: 4694) and under the "Basic Research Financing (Horizontal support of all Sciences)" call under the National Recovery and Resilience Plan "Greece 2.0" funded by the European Union − Next Generation EU (H.F.R.I. Project Number: 17007).

■ REFERENCES

(1) Ntziachristos, V. Fluorescence Molecular Imaging. *Annu. Rev. Biomed. Eng.* **2006**, *8*, 1−33.

(2) Hellebust, A.; Richards-Kortum, R. Advances in molecular imaging: Targeted optical contrast agents for cancer diagnostics. *Nanomedicine* **2012**, *7*, 429−445.

(3) Pu, K.; Shuhendler, A. J.; Jokerst, J. V.; Mei, J.; Gambhir, S. S.; Bao, Z.; Rao, J. Semiconducting Polymer Nanoparticles as Photoacoustic Molecular Imaging Probes in Living Mice. *Nat. Nanotechnol.* **2014**, *9*, 233−239.

(4) Zhu, C.; Liu, L.; Yang, Q.; Lv, F.; Wang, S. Water-Soluble Conjugated Polymers for Imaging, Diagnosis, and Therapy. *Chem. Rev.* **2012**, *112* (8), 4687−4735.

(5) Wu, C.; Chiu, D. T. Highly Fluorescent Semiconducting Polymer Dots for Biology and Medicine. *Angew. Chem., Int. Ed.* **2013**, *52* (11), 3086−3109.

(6) Wang, Y.; Feng, L.; Wang, S Conjugated Polymer Nanoparticles for Imaging, Cell Activity Regulation, and Therapy. *Adv. Funct. Mater.* **2020**, *29* (5), 1806818.

(7) McCabe-Lankford, E. E.; Brown, T. L.; Levi-Polyachenko, N. H. Assessing fluorescence detection and effective photothermal therapy of near-infrared polymer nanoparticles using alginate tissue phantoms. *Lasers Surg. Med.* **2018**, *50* (10), 1040−1049.
(8) McCarthy, B.; Cudykier, A.; Singh, R.; Levi-Polyachenko, N.; Soker, S. Semiconducting Polymer Nanoparticles for Photothermal Ablation of Colorectal Cancer Organoids. *Sci. Rep.* **2021**, *11* (1), 1532.
(9) Graham-Gurysh, E.; Kelkar, S.; McCabe-Lankford, E.; Kuthirummal, N.; Brown, T.; Kock, N. D.; Mohs, A. M.; Levi-Polyachenko, N. Hybrid Donor−Acceptor Polymer Particles with Amplified Energy Transfer for Detection and On-Demand Treatment of Breast Cancer. *ACS Appl. Mater. Interfaces* **2018**, *10*, 7697−7703.
(10) Rohatgi, C. V.; Harada, T.; Need, E. F.; Krasowska, M.; Beattie, D. A.; Dickenson, G. D.; Smith, T. A.; Kee, T. W. Low-Bandgap Conjugated Polymer Dots for Near-Infrared Fluorescence Imaging. *ACS Appl. Nano Mater* **2018**, *1* (9), 4801−4808.
(11) Gao, D.; Hu, D.; Liu, X.; Zhang, X.; Yuan, Z.; Sheng, Z.; Zheng, H. Recent Advances in Conjugated Polymer Nanoparticles for NIR-II Imaging and Therapy. *ACS Appl. Polym. Mater.* **2023**, *2* (10), 4241−4257.
(12) Koralli, P.; Nega, A. D.; Vagiaki, L. E.; Pavlou, A.; Siskos, M. G.; Dimitrakopoulou-Strauss, A.; Gregoriou, V. G.; Chochos, C. L. New Conjugated Polymer Nanoparticles with High Photoluminescence Quantum Yields for Far-red and Near Infrared Fluorescence Bioimaging. *Mater. Chem. Front.* **2020**, *4* (8), 2357−2369.
(13) Koralli, P.; Tsikalakis, S.; Goulielmaki, M.; Arelaki, S.; Muller, J.; Nega, A. D.; Herbst, F.; Ball, C. R.; Gregoriou, V. G.; Dimitrakopoulou-Strauss, A.; et al. Rational design of aqueous conjugated polymer nanoparticles as potential theranostic agents of breast cancer. *Mater. Chem. Front.* **2021**, *5* (13), 4950−4962.
(14) Biczók, L.; Bérces, T. Temperature Dependence of the Rates of Photophysical Processes of Fluorenone. *J. Phys. Chem.* **1988**, *92* (13), 3842−3845.
(15) Panigrahi, S. K.; Mishra, A. K. Inner Filter Effect in Fluorescence Spectroscopy: As a Problem and as a Solution. *J. Photochem. Photobiol. C* **2019**, *41*, 100318.
(16) Crosby, G. A.; Demas, J. N. The Measurement of Photoluminescence Quantum Yields. A Review. *J. Phys. Chem.* **1971**, *75* (8), 991−1024.
(17) Frisch, M. J.; Trucks, G. W.; Schlegel, H. B.; Scuseria, G. E., et al. *Gaussian 09, Revision D.01*; Gaussian, Inc.: Wallingford, CT, 2009.
(18) Lee, C.; Yang, W.; Parr, R. G. Development of the Colle−Salvetti Correlation-Energy Formula into a Functional of the Electron Density. *Phys. Rev. B* **1988**, *37*, 785−789.
(19) Wiberg, K. B., *Ab Initio Molecular Orbital Theory*; Hehre, W. J.; Radom, L.; Schleyer, P. V. R.; Pople, J. A. Eds.; Wiley: New York, 1986. DOI: .
(20) Samuels, Y.; Diaz, L. A., Jr.; Schmidt-Kittler, O.; Cummins, J. M.; DeLong, L.; Cheong, I.; Rago, C.; Huso, D. L.; Lengauer, C.; Kinzler, K. W.; et al. Mutant PIK3CA Promotes Cell Growth and Invasion of Human Cancer Cells. *Cancer Cell.* **2005**, *7* (6), 561−573.
(21) Bellou, S.; Hink, M. A.; Bagli, E.; Panopoulou, E.; Bastiaens, P. I. H.; Murphy, C.; Fotsis, T.; et al. VEGF Autoregulates Its Proliferative and Migratory ERK1/2 and p38 Cascades by Enhancing the Expression of DUSP1 and DUSP5 Phosphatases in Endothelial Cells. *Am. J. Physiol. Cell Physiol.* **2009**, *297* (6), C1477−C1489.
(22) Bagli, E.; Stefaniotou, M.; Morbidelli, L.; Ziche, M.; Psillas, K.; Murphy, C.; Fotsis, T. Luteolin Inhibits Vascular Endothelial Growth Factor-Induced Angiogenesis; Inhibition of Endothelial Cell Survival and Proliferation by Targeting Phosphatidylinositol 3′-Kinase Activity. *Cancer Res.* **2004**, *64* (21), 7936−7946.
(23) Jaffe, E. A.; Nachman, R. L.; Becker, C. G.; Minick, C. R. Culture of Human Endothelial Cells Derived from Umbilical Veins. Identification by Morphologic and Immunologic Criteria. *J. Clin. Invest.* **1973**, *52* (11), 2745−2756.
(24) Panopoulou, E.; Gillooly, D. J.; Wrana, J. L.; Zerial, M.; Stenmark, H.; Murphy, C.; Fotsis, T. Early Endosomal Regulation of Smad-Dependent Signaling in Endothelial Cells. *J. Biol. Chem.* **2002**, *277* (20), 18046−18052.
(25) Carlsson, S. R.; Fukuda, M. The Polylactosaminoglycans of Human Lysosomal Membrane Glycoproteins Lamp-1 and Lamp-2. Localization on the Peptide Backbones. *J. Biol. Chem.* **1990**, *265* (34), 20488−20495.
(26) Pols, M. S.; Klumperman, J. Trafficking and Function of the Tetraspanin CD63. *Exp. Cell Res.* **2009**, *315* (9), 1584−1592.
(27) Mura, M.; Hatherley, D.; Knapp, S.; Davies, A. M.; Siebold, C. Structural Basis for Ca2 ± Dependent Recognition of Nonself Glycans by Lectin RegIII*β*. *Biochem. J.* **2019**, *476* (13), 1889−1906.
(28) Mochly-Rosen, D.; Das, K.; Grimes, K. V. Protein Kinase C, an Elusive Therapeutic Target? *Nat Rev Drug Discov.* **2012**, *11*, 937−957.
(29) Wang, S.; Liu, Z.; Tong, Y.; Zhan, Y.; Zhou, Y.; Wang, F.; Zhang, Y.; Zheng, W.; Yang, Z.; Li, L.; et al. Engineering Fluorophores with NIR-II Emission and High Brightness for In Vivo Biological Imaging. *Nat. Nanotechnol.* **2022**, *17* (4), 496−505.

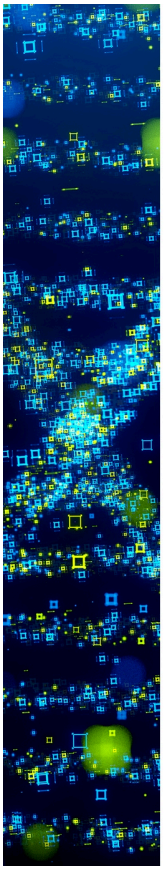

https://doi.org/10.1021/acs.macromol.5c01788
Macromolecules 2026, 59, 1429−1442